

SCIENTIFIC REPORTS



OPEN

Bi-2212/1T-TaS₂ Van der Waals junctions: Interplay of proximity induced high- T_c superconductivity and CDW order

Ang J. Li , Xiaochen Zhu, G. R. Stewart & Arthur F. Hebard 

Understanding the coexistence, competition and/or cooperation between superconductivity and charge density waves (CDWs) in the transition metal dichalcogenides (TMDs) is an elusive goal which, when realized, promises to reveal fundamental information on this important class of materials. Here, we use four-terminal current-voltage measurements to study the Van der Waals interface between freshly exfoliated flakes of the high- T_c superconductor, Bi-2212, and the CDW-dominated TMD layered material, 1T-TaS₂. For highly transparent barriers, there is a pronounced Andreev reflection feature providing evidence for proximity-induced high- T_c superconductivity in 1T-TaS₂ with a surprisingly large energy gap (~20 meV) equal to half that of intrinsic Bi-2212 (~40 meV). Our systematic study using conductance spectroscopy of junctions with different transparencies also reveals the presence of two separate boson modes, each associated with a “dip-hump” structure. We infer that the proximity-induced high- T_c superconductivity in the 1T-TaS₂ is driven by coupling to the metastable metallic phase coexisting within the Mott commensurate CDW (CCDW) phase and associated with a concomitant change of the CCDW order parameter in the interfacial region.

In the past few decades, the study of interfaces between novel materials including metals, semiconductors, superconductors, topological insulators and layered materials harboring charge density waves (CDWs) has generated the emergence of unexpected phenomena. These discoveries require a new understanding of underlying mechanisms which in turn may well lead to promising new technologies. The proximity effect at the superconducting/normal (S/N) boundary posits a leakage of Cooper pairs into the normal metal accompanied by the appearance of superconductivity at the interface and extending into the metal^{1–3}. Specifically, detailed study of S/N proximity junctions provides a unique probe of the pairing interaction of both conventional¹ and unconventional² superconductors. The reflection of an electron in N as a hole of opposite wave vector (Andreev reflections) and propagation of paired quasiparticles in S gives rise to phenomena including contact-dependent excess conductance, reduced energy gaps and lower transition temperatures on both sides of the interface. Van der Waals (VdW) interfaces advantageously reduce concerns about epitaxial matching across the interface and have already been studied using ultra-smooth cleavable superconductors such as: Bi-2212 in contact with the topological insulators, Bi₂Se₃ and Bi₂Te₃⁴, 2H-NbSe₂ in contact with Bi₂Se₃⁵ and 2H-NbSe₂ in contact with graphene⁶.

In this paper we are motivated by the question of how coexistence, competition or cooperation of superconductivity with various collective electronic states, in particular charge density wave ordered states, can be studied using the proximity effect. This question has been discussed in systems of reduced dimensionality which are prone to electronic instabilities, such as the *coexistence* of CDW order and superconductivity in 2H-NbSe₂⁷ in contrast to the *competition* of CDW order and superconductivity in, for example, Yttrium cuprate⁸. The quasi-two dimensional layered transition-metal dichalcogenides (TMDs), many of which harbor CDW order, have served as model systems for the investigation of the interplay between CDWs and low T_c superconductivity where low- T_c superconductivity can be achieved by the application of pressure⁹ to pristine 1T-TaS₂ or by partial substitution of Se for S¹⁰, Fe for Ta¹¹ or electric-field gate controlled intercalation of Li¹² and is always associated with the more conducting nearly commensurate CDW (NCCDW) phase and even the higher temperature incommensurate

Department of Physics, University of Florida, Gainesville, FL, 32611, USA. Correspondence and requests for materials should be addressed to A.F.H. (email: afh@phys.ufl.edu)

CDW (ICCDW) phase. Interestingly, in the pressure experiments on pristine 1T-TaS₂, the low- T_c superconductivity ($T_c \approx 5$ K) persists until the pressure is high enough to convert the CDW phase to a metal⁹.

The TMD, 1T-TaS₂, is a particularly interesting CDW material for such studies because it exhibits a pronounced first order CDW transition with hysteretic resistance transitions in the 180–230 K temperature range. It is generally recognized that electron–electron as well as electron–phonon interactions in 1T-TaS₂^{13–16} are responsible for the evolution of a nearly commensurate CDW (NCCDW) to a Mott commensurate CDW (CCDW) phase dominating at low temperatures. Two opposing arguments focus on where and how low T_c superconductivity forms in 1T-TaS₂. The first argues that the superconductivity is formed within the metallic interdomain spaces separating the CCDW domains where tens of “star of David” clusters clump into rough hexagonal domains reproducing the Mott-CCDW phase locally^{9,10}. The second argues that the superconductivity, characterized by a shallow electron pocket at the Brillouin-zone center, is formed exactly within the clusters of stars¹¹ in the NCCDW phase in real space. We note that low- T_c superconductivity at ambient pressure is only found in non-pristine (i.e., doped) 1T-TaS₂ where the NCCDW phase dominates.

In this study, we find evidence for proximity-induced high- T_c superconductivity in the topmost layers of pristine 1T-TaS₂ at the interface of Van der Waals bonded Bi-2212/1T-TaS₂ junctions, where pristine Bi-2212 is the high- T_c superconductor Bi₂Sr₂CaCu₂O_{8+ δ} with a transition temperature $T_c = 85$ K and intrinsic energy gap $\Delta_0 = 40$ meV. Andreev reflection, marked by excess current and a wide zero-bias conductance peak, is observed at temperatures up to 80 K where the 1T-TaS₂ is in the Mott-CCDW state. The proximity induced gap Δ_a in the 1T-TaS₂ is found to be a surprisingly large 20 meV, thereby implying a strong coupling limit ($2\Delta_a/k_B T_c \sim 5.8$) instead of the BCS weak coupling limit of 3.5. In addition to the induced gap in the 1T-TaS₂, we also observe a depressed gap compared to the intrinsic gap Δ_0 in the vicinity of the interface on the Bi-2212 side.

Our observation of a transparency-dependent superconducting proximity effect of Bi-2212/1T-TaS₂ junctions strongly indicates that superconductivity is induced in a metallic phase of 1T-TaS₂. The transparency is defined as a dimensionless normal conductance, $\sigma_N = \frac{1}{1+Z^2}$, where the parameter Z is extracted from theoretical fitting of conductance spectroscopy data using the extended BTK model described below. Such a finding is somewhat surprising since, in the absence of intimately contacting Bi-2212, pristine 1T-TaS₂ is in an insulating CCDW state, and a proximity effect is only expected to occur in metallic systems. The puzzle here is that at the temperatures where Bi-2212 is superconducting, the stoichiometric pure 1T-TaS₂ is in the nonmetallic Mott-CCDW state and a proximity effect is in fact observed thereby implying that the proximity of the Bi-2212 induces changes in the CDW order parameter to achieve a more metallic phase. Said in another way, the mutual interaction of the CDW and superconducting order parameters is such that the proximity-induced gap in the 1T-TaS₂ can only appear if the CDW order parameter is changed in the interfacial region as is the superconducting gap associated with the Bi-2212. This interpretation is consistent with evidence for a metastable metallic phase, induced by voltage pulses, laser pulses or current excitations, residing within the Mott-CCDW phase^{17–21}. This metastable state is ascribed to the reduction of onsite Coulomb interaction U and increase of Hubbard band width W via phase shifts of the CDW order parameter or interplay between the electron–electron and electron–phonon interactions in the topmost layers^{17–21}.

The superconducting proximity effect, attributed to the leakage of Cooper pairs into a conducting metallic phase of the 1T-TaS₂, is also confirmed by the good agreement of our c -axis conductance spectroscopy (dI/dV vs. V) with an extended BTK model for d -wave superconductors²². Additionally, our conductance measurements reveal the presence of two dip–hump structures which can be interpreted to reflect an inherent electron–phonon interaction in 1T-TaS₂ that assists the formation of high- T_c superconductivity in the metastable metallic domains residing within the Mott-CCDW phase. This evidence of electron–phonon interaction assisted high- T_c superconductivity within the Mott CCDW phase of 1T-TaS₂, presents a new paradigm for understanding the correlation of CDW order and high- T_c superconductivity in 1T-TaS₂.

Results

Characteristics of Samples. Nearly optimally doped crystals of high- T_c cuprate Bi₂Sr₂Ca₁Cu₂O_{8+ δ} (Bi-2212) and stoichiometrically pure layered transition metal dichalcogenide (TMD) 1T-TaS₂ crystals were used. The critical superconducting temperature T_c of Bi-2212 (Supplementary Fig. S.1(a)) and the CCDW–NCCDW phase transition temperatures on cooling/warming processes (Supplementary Fig. S.1(b)) were verified with AC transport measurements to be at 85 K and 180 K/230 K respectively.

The Bi-2212 and 1T-TaS₂ crystals were mechanically exfoliated in a dry atmosphere as thin flakes with approximately rectangular shapes and nominal thicknesses of 0.5–2.0 μm and 2.0–5.0 μm for the Bi-2212 and 1T-TaS₂ flakes respectively. The cleaved surfaces were clean and flat, with a mean roughness of 1.55 Å for Bi-2212 and 1.52 Å for 1T-TaS₂ from AFM images as shown in Fig. 1(c). Two cleaved thin flakes were placed against each other and naturally bonded via Van der Waals forces²³; high quality normal metal–superconductor (NS) or normal metal–insulator–superconductor (NIS) junctions were then formed. Four terminal tunnel junction configurations with perpendicularly oriented top and bottom electrodes shown in the Fig. 1(d) schematic have the advantage that contact resistances are eliminated and the active area common to both electrodes (0.2 mm²) can be accurately calculated^{24,25}. Advantageously the c -axis of both the bottom (Bi-2212) and top (1T-TaS₂) electrodes are perpendicular to the substrate and thus colinear, thereby minimizing currents flowing along the ab -plane. Our c -axis conductance spectroscopy measurements were performed in a Quantum Design Physical Properties Measurement System (PPMS) at temperatures ranging from 2.5 K to 120 K. Using this set up we find the intrinsic Bi-2212 superconducting gap to be in the range 38 to 42 meV for both Bi-2212/1T-TaS₂ junctions (see below) and Bi-2212/graphite (Supplementary Fig. S.2) junctions, in good agreement with previous point-contact tunneling studies on single crystal Bi-2212^{26,27}.

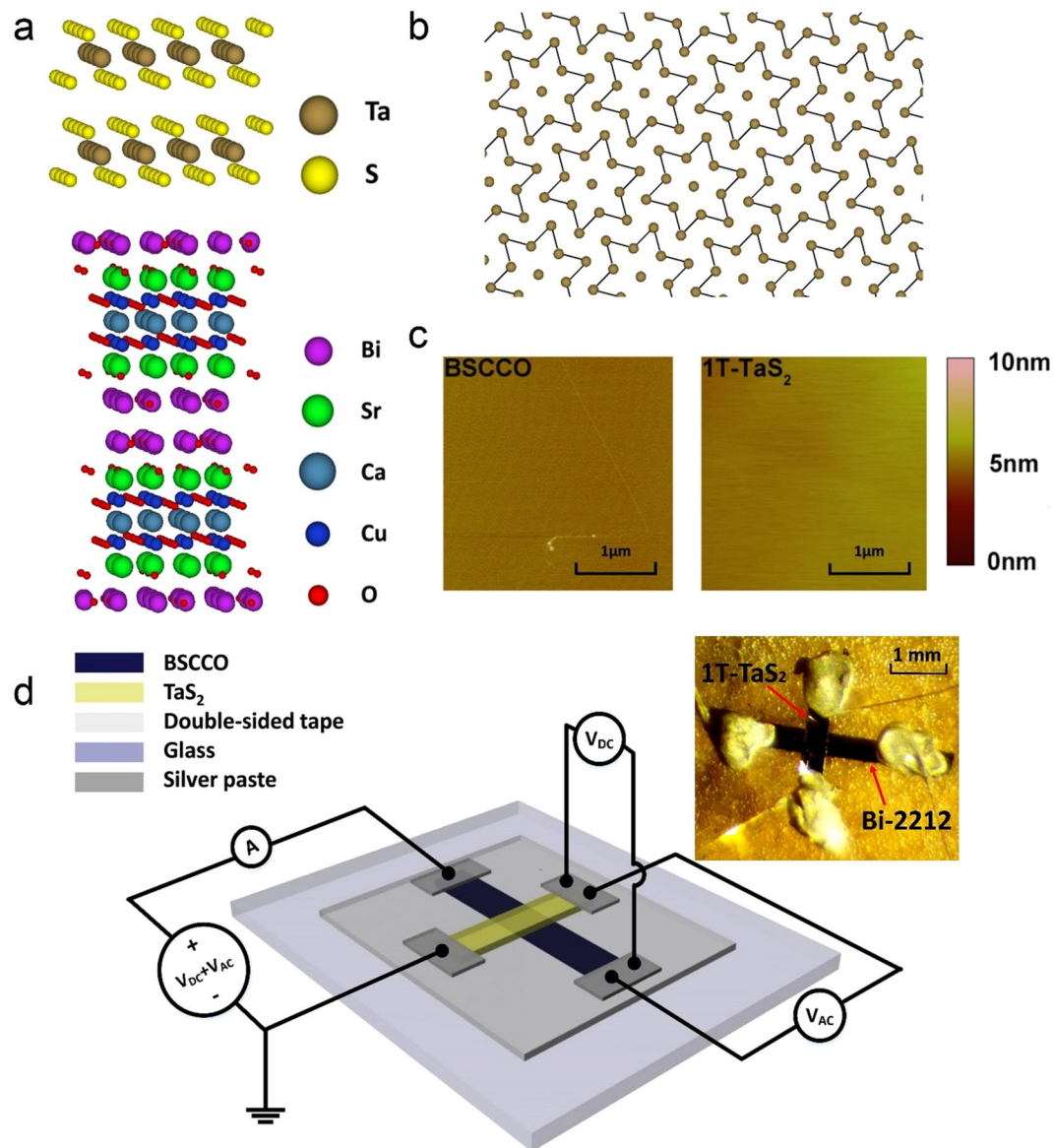


Figure 1. Sample characteristics and measurement set-up. **(a)** Crystal structure of 1T-TaS₂ (upper schematic) and Bi-2212 (lower schematic) viewed along the direction parallel to the *ab*-plane. **(b)** Schematic of monolayer 1T-TaS₂ along the *c*-axis in CCDW state. The interlocked clusters of Ta atoms (“star of David”) are sketched in dark yellow for the Ta atoms and the chemical bonds between Ta atoms, excluding the central one, are sketched in black. The S atoms are not shown. **(c)** Atomic force microscope (AFM) images of the cleaved surfaces for thin flakes of Bi-2212 (left) and 1T-TaS₂ (right). The scale bar corresponds to 1 μm. The surface mean roughness of thin flake Bi-2212 and 1T-TaS₂ are 1.55 Å and 1.52 Å respectively. **(d)** Schematic depicting experimental set-up for making four-terminal current-voltage and differential conductance vs voltage measurements using an AC + DC adder in conjunction with one DC voltmeter and two synchronized lock-in amplifiers, one for AC current and the other for AC voltage. Inset: photograph of Bi-2212/1T-TaS₂ device. The scale bar corresponds to 1 mm.

Experimental measurements of Bi-2212/1T-TaS₂ junctions. *Highly transparent junctions.* *C*-axis AC differential conductance spectroscopies and DC current-voltage (*I*–*V*) characteristics were measured on Bi-2212/1T-TaS₂ junctions. To exemplify the superconducting proximity effect at the interface, junctions with high transparency^{1,3,28,29} or low *Z* parameter described in the BTK model²⁹ are needed. Under these conditions, Cooper pairs in the superconductor (S) can leak into the normal material (N) side resulting in a spatially dependent superconducting gap $\Delta(x)$ that extends across the interface along the *c*-axis and into the 1T-TaS₂. Various gap features can be identified beginning with the intrinsic superconducting gap $\Delta_0 = 40$ mV deep in the superconductor which decreases to a depressed superconducting gap $\Delta_p = 28$ mV at the S/N interface and then decreases to a proximity effect induced superconducting gap $\Delta_a = 20$ mV on the N side of the interface which decreases in magnitude with increasing distance from the interface^{1,3}. Moreover, the different proximity region widths

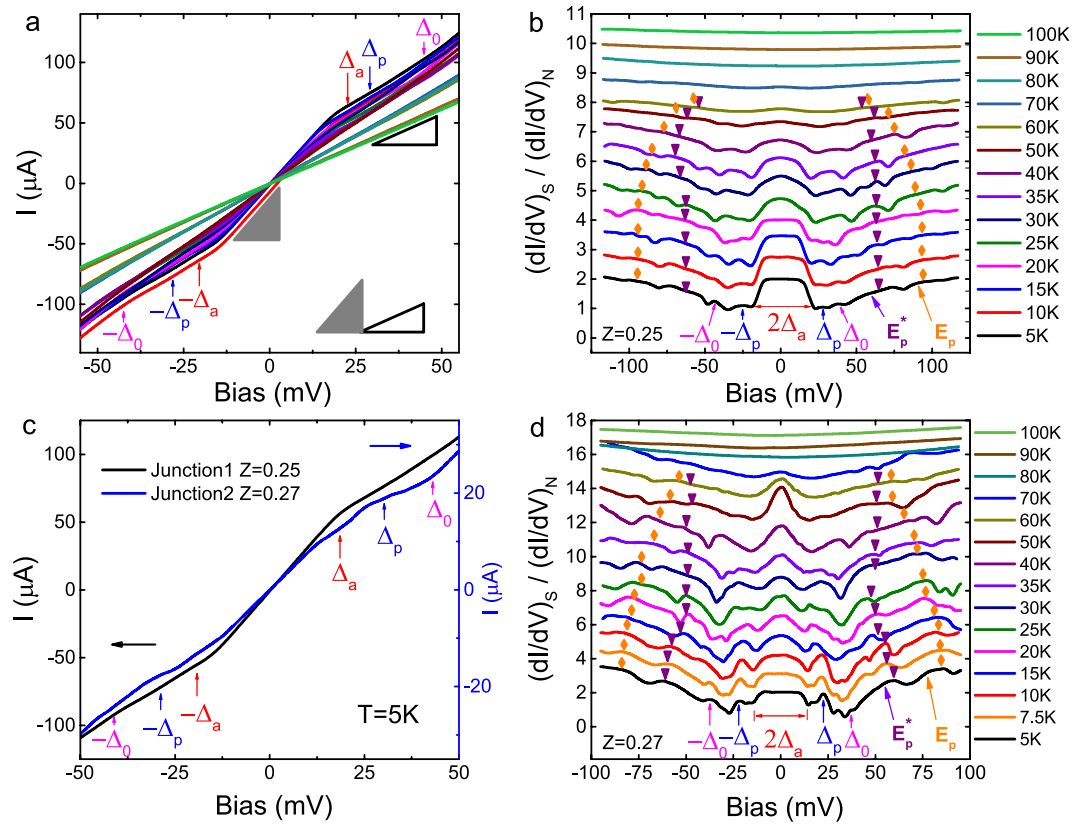


Figure 2. Highly transparent Bi-2212/1T-TaS₂ junctions. **(a)** DC I - V curves of Junction-1, with BTK parameter $Z = 0.25$, at various temperatures from 5 K to 100 K. Δ_a (Red), Δ_p (Blue) and Δ_0 (Magenta) respectively represent the induced superconducting gap on 1T-TaS₂ side at interface, the depressed superconducting gap on Bi-2212 side at interface, and the intrinsic superconducting gap of Bi-2212. The hollow solid triangle indicates the normal current of the junction, where the normal conductance at low temperatures in the superconducting state is approximately equal to that of the normal state. The solid gray triangle indicates the excess current due to Andreev reflection at N-S interface, where the conductance within the Andreev reflection region amounts to nearly twice the normal state conductance well below T_c . **(b)** Normalized AC differential conductance $(dI/dV)_S/(dI/dV)_N$ for Junction-1, where the differential conductance at 100 K is considered as the normal state conductance. The curves are shifted for clarity. **(c)** DC I - V curves of Junction-1 ($Z = 0.25$, black) and Junction-2 ($Z = 0.27$, blue) at 5 K. The induced superconducting gap Δ_a and excess current within $\pm\Delta_a$ of Junction-2 are slightly lower relative to Junction-1. The normal conductance of Junction-2, around $0.62 \mu\text{A}/\text{mV}$, is lower than the normal conductance around $1.85 \mu\text{A}/\text{mV}$ for Junction-1. **(d)** AC differential conductance $(dI/dV)_S/(dI/dV)_N$ for Junction-2, normalized by the differential conductance at 100 K. Curves are shifted for clarity. Note: for panels **(b,d)**, the orange/purple markers and arrows are discussed in the text.

within which these gaps exist depend sensitively on the transparency of junctions^{1, 3, 30–32}. In addition, different quasi-particle lifetimes or scattering rates at the vicinity of interface might affect the spectroscopic line shapes³³.

DC current-voltage I - V curves of Junction-1, with BTK parameter $Z = 0.25$, show clear zero-bias excess current relative to the normal current (indicated by the red vertical arrows labeling the induced gap, $\pm\Delta_a$) as shown in Fig. 2(a) for temperatures from 5 K to 100 K. The slope within the excess current range from -20 meV to 20 meV at 5 K, as indicated by the solid gray triangle, is nearly twice the slope within the normal current range indicated by the solid hollow triangle. At temperatures well below the T_c (~ 85 K) of Bi-2212, the excess current in the vicinity of zero bias is approximately twice the normal current, and therefore attributable to Andreev reflection at the interface²⁹, where the electrons injected from N side are reflected as holes with time reversal symmetry tracing the injected electrons' track back into N side. To conserve current across the interface, Cooper pairs flow at the Fermi energy within S. These Cooper pairs have electron-like (ELQ) and hole-like (HLQ) quasiparticle character above/below the edges of the energy gap and the conversion process only occurs when the incident electrons on the N side lie within the conductance plateau defined over the energy range $\pm\Delta_a$ shown in the normalized differential conductance plot of Fig. 2(b).

The two additional nonlinear features marked as blue and magenta vertical arrows in Fig. 2 are attributed respectively to the two superconducting gaps Δ_p and Δ_0 mentioned at the beginning of this section. The AC differential conductance spectroscopies $(dI/dV)_S$ of Junction-1, normalized by the normal state conductance $(dI/dV)_N$ at 100 K, at various temperatures from 5 K to 100 K shown in Fig. 2(b) confirm the features observed from I - V curves. The proximity effect induced superconducting gap $\Delta_a = \pm 20$ meV at 5 K on the 1T-TaS₂ side of

	Z	$\tilde{\sigma}_N$ $\mu\text{A}/\text{mV}$	$\Delta_0^{\text{exp}}/\Delta_0^{\text{theory}}$ meV	$\Delta_p^{\text{exp}}/\Delta_p^{\text{theory}}$ meV	$\Delta_a^{\text{exp}}/\Delta_a^{\text{theory}}$ meV	Γ_0 meV	Γ_p meV	Γ_a meV	$U_{e\text{-ph}}/E_p$ meV	$U_{e\text{-ph}}^*/E_p^*$ meV	$d_S/d_{vdW}/d_N/\xi_0$
Junction-1	0.25	1.85	40/41.0	28/26.8	20/19.1	0.8	2.7	0.1	95/88	65/64	5.5/2/10
Junction-2	0.27	0.62	39/39.6	23/22.8	16/16.5	0.8	0.2	0.1	83/79	63/56	5/1.9/8
Junction-3	0.5	0.21	38/42.3	21/18.5	21/17.3	0.6	9.1	5.2	93/89	66/62	4.4/1.6/2
Junction-4	0.8	—	39/39.2	23/23.3	23/22.2	2.1	2.3	2.2	—	—	4/1.2/0.5
Junction-5	2.5	—	41/40.3	—	—	8.1	—	—	—	—	—
Bi-2212/graphite	1	55.62	42/40.5	—	—	6.1	—	—	—	—	—

Table 1. Parameters used in calculation (marked as “theory”) or from measurements (marked as “exp”) of the conductance spectroscopies at 5 K for various junctions. Z: BTK parameter; $\tilde{\sigma}_N$: normal conductance from measurement; Δ_0 : Bi-2212 intrinsic superconducting gap; Δ_p : suppressed superconducting gap on S side; Δ_a : proximity induced superconducting gap on N side; Γ_0 : quasiparticle lifetime parameter on S side; Γ_p : quasiparticle lifetime parameter at interface on S side; Γ_a : quasiparticle lifetime parameter at interface on N side; $U_{e\text{-ph}}/U_{e\text{-ph}}^*$: position of higher/lower energy scaled hump on conductance spectroscopy. E_p/E_p^* : position of higher/lower energy scaled peak/dip in positive/negative voltage regions of d^2I/dV^2 . $d_S/d_{vdW}/d_N/\xi_0$: thickness of proximity region on S side, Van der Waals stacking distance and thickness of proximity region on N side.

the interface delineates the voltage region within which Andreev reflection occurs. Additional gap features, relevant to the nonlinear features observed from I - V curves, are believed to be the density of states (DOS) features corresponding to the depressed superconducting gap Δ_p on the Bi-2212 side at the interface and the intrinsic superconducting gap Δ_0 of Bi-2212. For Junction-1, the sizes of the two gaps are $\Delta_p = 28$ meV and $\Delta_0 = 40$ meV respectively at 5 K. As temperature increases, the zero-bias conductance peak evolves from a flat mesa to a rounded hump while the peak's width and height are depressed up to temperatures near 80 K. The gaps, Δ_p and Δ_0 merge with increasing temperature until all gaps disappear near 80 K. Similar features are also observed on Junction-2 with BTK parameter $Z = 0.27$, as shown in Fig. 2(c) inset for DC I - V curves and (d) for AC differential conductance spectroscopies.

Both Junction-1 and Junction-2 show characteristics of highly transparent junctions, exhibiting high normal state conductance of $1.85 \mu\text{A}/\text{mV}$ and $0.62 \mu\text{A}/\text{mV}$ at 5 K respectively as shown in Fig. 2. As revealed by the conductance spectroscopies of Junction-2 (seen in Fig. 2(d)), the sizes of the three gaps $\Delta_0 = 39$ mV, $\Delta_p = 23$ mV and $\Delta_a = 16$ mV at 5 K are close to the values of Junction-1. The consistency of the Bi-2212 intrinsic superconducting gap size measured for Junction-1 and Junction-2 with previous c -axis point-contact tunneling studies on single crystal Bi-2212^{26,27} is satisfying. Any variation of the differential conductance spectroscopies' line-shape for Junction-1 and Junction-2 might be ascribed to the discrepancy of proximity regions' width and scattering rate of quasiparticles at the vicinity of the interface^{1,3,30-33}.

Andreev reflection such as observed here for our low-Z junctions (Junction-1 and Junction-2) exists at the normal metal-superconductor (N-S) interface, thereby indicating that the observed Andreev reflection feature on our Bi-2212/1T-TaS₂ junctions implies at minimum a metallic component on the N side. We conclude that the metastable metallic phase of 1T-TaS₂ residing in the Mott-CCDW state at low temperatures and revealed by STM studies¹⁷⁻²¹ is the requisite metallic state for proximity coupling to pristine 1T-TaS₂, where the metallic phase has a smaller parameter U/W than the Mott-CCDW phase. Importantly, the Andreev enhanced zero-bias peak disappearing at high temperature around 80 K in Junction-1 and Junction-2 reflects *proximity induced high- T_c superconductivity* in the metastable metallic phase residing in the layers of 1T-TaS₂ which are adjacent to the Bi-2212.

Besides the evidence for a robust superconducting proximity effect existing in our two low-Z Bi-2212/1T-TaS₂ junctions, we find two dip-hump structures positioned at $U_{e\text{-ph}}$ and $U_{e\text{-ph}}^*$ for both junctions, which are indicated at their respective peaks (humps) by orange diamond and purple inverted triangles in Fig. 2(b,d). As suggested by neutron resonance and ARPES results^{34,35}, a single dip-hump structure in Bi-2212 probably stems from the electron-boson coupling, or combined electron-boson coupling and pseudogap³⁶ corresponding to a boson mode energy Ω . As the *fingerprint* of a boson mode, the energy at the maximum slope of the dip-hump structure in conductance spectroscopies or the peak/dip in the dI^2/dV^2 spectra at positive/negative bias regions for NIS junctions is positioned at $E_p = \Delta_0 + \Omega$ ³⁷⁻⁴⁰. Indicated by orange and purple arrows for the lowest temperatures in Fig. 2(b,c) respectively in the conductance spectroscopies, the determination of experimental values of E_p and E_p^* from dI^2/dV^2 spectra are described in Fig. S.4 of Supplementary information. Consequently, with the information summarized in Table 1 at 5 K, the boson mode energies referred to the two dip-hump structures are $\Omega = E_p - \Delta_0 = 48$ meV and $\Omega^* = E_p^* - \Delta_0 = 24$ meV for Junction-1 with $\Delta_0 = 40$ meV; $\Omega = 40$ meV and $\Omega^* = 17$ meV for Junction-2 with $\Delta_0 = 39$ meV. For intrinsic Bi-2212, the boson mode energy found in STM spectra is around 52 ± 8 meV⁴¹, leading us to conclude that the hump peaked at $U_{e\text{-ph}}$ is from intrinsic Bi-2212 accompanied by a boson mode energy Ω , while the hump peaked at $U_{e\text{-ph}}^*$ is a heretofore unseen hump due to another boson mode with lower energy Ω^* . As temperature increases, the two humps merge to a single hump near 50–60 K for both junctions, a temperature somewhat more than the temperature near 40 K where Δ_0 and Δ_p merge as shown in the differential conductance spectroscopies in Fig. 2(b,d).

Two boson modes. Our Bi-2212/1T-TaS₂ Junction-3, with slightly lower transparency (BTK parameter $Z = 0.5$), offers more information about the dip-hump structures observed in Junction-1 and Junction-2. As shown in

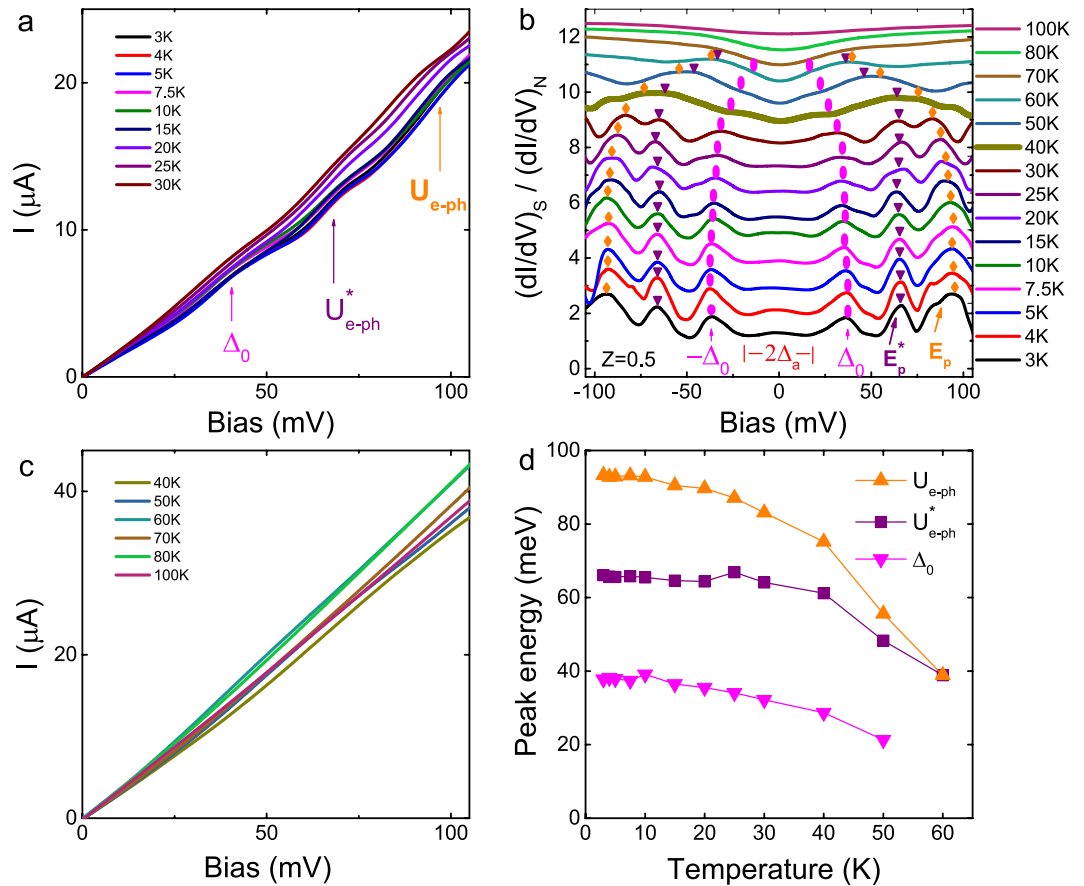


Figure 3. Bi-2212/1T-TaS₂ junction with BTK $Z=0.5$ (Junction-3). **(a)** DC I - V curves of Junction-3, with BTK parameter $Z=0.5$, at various temperatures from 3 K to 30 K, well below the T_c of Bi-2212. The Bi-2212 intrinsic superconducting gap Δ_0 is indicated by a magenta vertical arrow. U_{e-ph} and U_{e-ph}^* correspond to the peak energy positions of two nonlinear features due to the two boson modes measured with respect to Δ_0 . The normal conductance decreases with temperature, where the normal conductance at 5 K for Junction-3 is around $0.21 \mu\text{A}/\text{mV}$. **(b)** Normalized AC differential conductance $(dI/dV)_S/(dI/dV)_N$ for Junction-3. The differential conductance at 100 K manually scaled into the range of the conductance at one specific temperature serves as the normal conductance. Relative to the NS Andreev reflection feature seen in Junction 1 and 2, the zero-bias excess differential conductance peak is significantly reduced and almost disappears at around 40 K. The Bi-2212 intrinsic superconducting gap Δ_0 and the humps referring to boson modes with energies Ω^* and Ω are indicated respectively by solid magenta ellipses, inverted purple triangles and orange diamonds. Positions of E_p and E_p^* are marked by orange and purple arrows. The curves are shifted for clarity. **(c)** DC I - V curves of Junction-3 at various temperatures from 40 K to 100 K. The conductance in the normal state at 100 K is around $0.4 \mu\text{A}/\text{mV}$. The temperature dependence of the conductance for Junction-3 evolves consistently with intrinsic 1T-TaS₂ at temperatures from 3 K to 100 K shown in Fig. S.1(b). **(d)** Temperature dependence of the two humps' peak positions and the Bi-2212 superconducting gap.

Fig. 3(a), the DC I - V curves at various temperatures (3 K to 30 K) well below Bi-2212 T_c show several nonlinear features. Besides the nonlinear feature of the Bi-2212 intrinsic superconducting gap Δ_0 indicated by the magenta vertical arrow, the other two nonlinear features taking place above Δ_0 , as indicated by the purple and orange vertical arrows, are also clearly observed. Junction-3 with lower normal conductance around $0.21 \mu\text{A}/\text{mV}$ at 5 K than Junction-1 and Junction-2, however, demonstrates the normal conductance varies with temperatures indicating the 1T-TaS₂ for Junction-3 might behave more like a Mott-CCDW material rather than the metastable metallic material in the more transparent junctions. The temperature dependence of normal conductance in Junction-3, referring to a less metallic NS junction, probably originates from the carrier delocalization in the Mott-insulating state in 1T-TaS₂ with increasing temperature¹³⁻¹⁶.

The normalized AC differential conductance spectroscopies $(dI/dV)_S/(dI/dV)_N$ of Junction-3, obtained using the method described in the Methods section, at various temperatures from 3 K to 100 K are shown in Fig. 3(b). A strongly suppressed amplitude of the zero-bias peak for Junction-3 relative to Junction-1 and Junction-2 is observed. Such strong suppression suggests a stronger scattering rate or shorter quasiparticle lifetimes in the proximity-effect-induced superconducting region on the 1T-TaS₂ side at interface. The width of the zero-bias peak decreases with increasing temperature, and is totally suppressed near 40 K. Meanwhile, the feature representing the depressed superconducting gap Δ_p is clearly not observed, as seen in Fig. 3(b), which we ascribe to the

closer proximity between Δ_p and Δ_a and temperature broadening. For Junction-3, the measured superconducting gap Δ_0 around 38 meV at 5 K is slightly smaller but still consistent with the highly transparent Junction-1 and Junction-2. Notably, the width of zero-bias peak is around 21 meV, which is not strongly depressed relative to Junction-1 and Junction-2.

Sharper and clearer signatures of two dip-hump structures are observed in Junction-3. The conductance spectroscopy indicates the hump (peak marked by the orange diamond) due to the boson mode energy Ω has a broader width than the hump (peak marked by the purple inverted triangle) due to the boson mode energy Ω^* . The two humps of Junction-3 at 5 K which are peaked at the energy $U_{e-ph} = 93$ meV and $U_{e-ph}^* = 66$ meV, as well as the maximum slope positions of dip-hump structures $E_p = 89$ meV and $E_p^* = 62$ meV are listed in Table 1, which correspond to the boson mode energies $\Omega = E_p - \Delta_0 = 89 - 38 = 51$ meV and $\Omega^* = E_p^* - \Delta_0 = 62 - 38 = 24$ meV. More details about the temperature evolution (at temperatures below Bi-2212 T_c) of the Bi-2212 superconducting gap Δ_0 and two humps are presented in Fig. 3. Similar to the highly transparent Junction 1 and 2, the two humps merge toward each other with increasing temperature, and almost merge into a single hump at an energy position of $U_{e-ph} = U_{e-ph}^* = 39$ meV at around 60 K. The zero-bias conductance peak is totally suppressed at a lower temperature around 40 K instead of 80 K as in Junction 1 and 2; however, still indicating proximity-induced high- T_c superconductivity in 1T-TaS₂.

Theoretical modeling and results. The superconducting proximity effect distinguishes two major regimes at the interface of NS or NIS junctions^{1,3}. The NS interface for electrons with energy $E < \Delta_a$ injected from the N side is the boundary between the induced superconducting region and the normal material on the N side, whereas electrons within energy $\Delta_a < E < \Delta_p$ and $\Delta_p < E < \Delta_0$ will experience the NS interface from the S side. Two schemes of a proximity junction with thicknesses of the proximity regions on the S and N sides respectively marked as d_S and d_N are depicted in Fig. 4(a). Schemes Nos. 1 and 2 correspond respectively to the cases $\Delta_0 > \Delta_p > \Delta_a$ and $\Delta_0 > \Delta_p \sim \Delta_a$.

The c -axis conductance characteristics of various junctions, including Bi-2212/1T-TaS₂ and Bi-2212/graphite junctions, are calculated based on an extended BTK model of the tunneling spectrum for anisotropic superconductors²². For Bi-2212, with d -wave symmetry of the superconducting gap^{42–44}, the electron-like quasiparticle (ELQ⁺) and hole-like quasiparticle (HLQ⁻) experience the same pairing potential, $|\Delta_+| = |\Delta_-| = \Delta_0 \cos(2\alpha)$, where the angle α in the plane perpendicular to the c -axis is a measure of the gap lobe's orientation and global phase $\phi_+ = \phi_- = 0$ along the c -axis. Then, the c -axis normalized differential conductance $(dI/dV)_S/(dI/dV)_N$ is expressed as

$$\frac{(dI/dV)_S}{(dI/dV)_N}(V) = \int_{-\infty}^{+\infty} \frac{\partial f_0(E - eV)}{\partial(eV)} \sigma_T(E) dE, \quad (1)$$

where $f_0(E)$ is the Fermi-Dirac distribution at temperature T . The dimensionless tunneling conductance at an energy E away from E_F is described as

$$\sigma_T(E) = \frac{\int_{\Omega} [1 + R_{eh}^2(E) - R_{ee}^2(E)] \sigma_N \cos \theta d\Omega}{\int_{\Omega} \sigma_N \cos \theta d\Omega}. \quad (2)$$

Equation (2) corresponds to a semi-spherical solid angle integration over the Fermi surface of d -wave superconductors. In the case of no mismatch of the Fermi level across the interface, the dimensionless normal conductance or transparency of the interface is $\sigma_N = \frac{1}{1+Z^2}$ as mentioned earlier. The rate of Andreev reflection (AR) $R_{eh}(E)$ and ordinary reflection (OR) $R_{ee}(E)$, based on the extended BTK model²², are expressed in equation (S.5) in Supplementary information. Additionally, by simply adding an imaginary energy term $-i\Gamma$ (as the quasiparticle lifetime parameter) to $E \rightarrow E - i\Gamma$ and $\Omega_{\pm} \rightarrow \sqrt{(E - i\Gamma)^2 - \Delta_0^2}$, the smearing effect on tunneling spectroscopy due to quasiparticle life time τ_R or scattering rate $1/\tau_R$ is quantitatively described^{33,45}.

The calculated conductance spectroscopies for various junctions show good agreement with measurement results, as shown in Fig. 4(b) for various junctions at 5 K, as well as the temperature-dependent conductance spectroscopies below Bi-2212 T_c for Bi-2212/1T-TaS₂ and Bi-2212/graphite junctions seen in Fig. S.3(a–e). Figure 4(c) also compares the temperature dependent gaps (Δ_0 , Δ_p and Δ_a) with theoretical calculations for various Bi-2212/1T-TaS₂ junctions. These calculations were only carried out up to 40 K because of high temperature smearing effects. The parameters used in calculation of the conductance characteristics at 5 K for various junctions are listed in Table 1. More details on theoretical modeling are described in Supplementary information (Section: Supplementary Discussion–Theoretical Modeling).

Discussion

The normalized differential conductance plots, as shown in Fig. 5(a), at temperatures from 5 K to 30 K for Bi-2212/1T-TaS₂ Junction-4 with BTK parameter $Z = 0.8$ exhibit the proximity effect described by Scheme No. 2 in Fig. 4(a). For this case there is no discontinuity in the gap at the interface (i.e., $\Delta_p = \Delta_a$). For even lower transparency interfaces, such as Junction-5 with BTK parameter $Z = 2.5$ shown in Fig. 5(b), any remnants of a superconducting proximity effect with markers at Δ_p and Δ_a have disappeared. To briefly summarize, for relatively high transparent Bi-2212/1T-TaS₂ Junction 1–4, the superconducting proximity effect is clearly experimentally observed (seen in Figs 2, 3 and 5(a)) via c -axis conductance spectroscopies. The temperature dependence of the gaps Δ_0 , Δ_p and Δ_a for Junction 1–4, displayed in the four panels of Fig. 4(c), show a merging of Δ_p and Δ_a with decreasing transparency (or increasing Z) of the interface and increasing temperature.

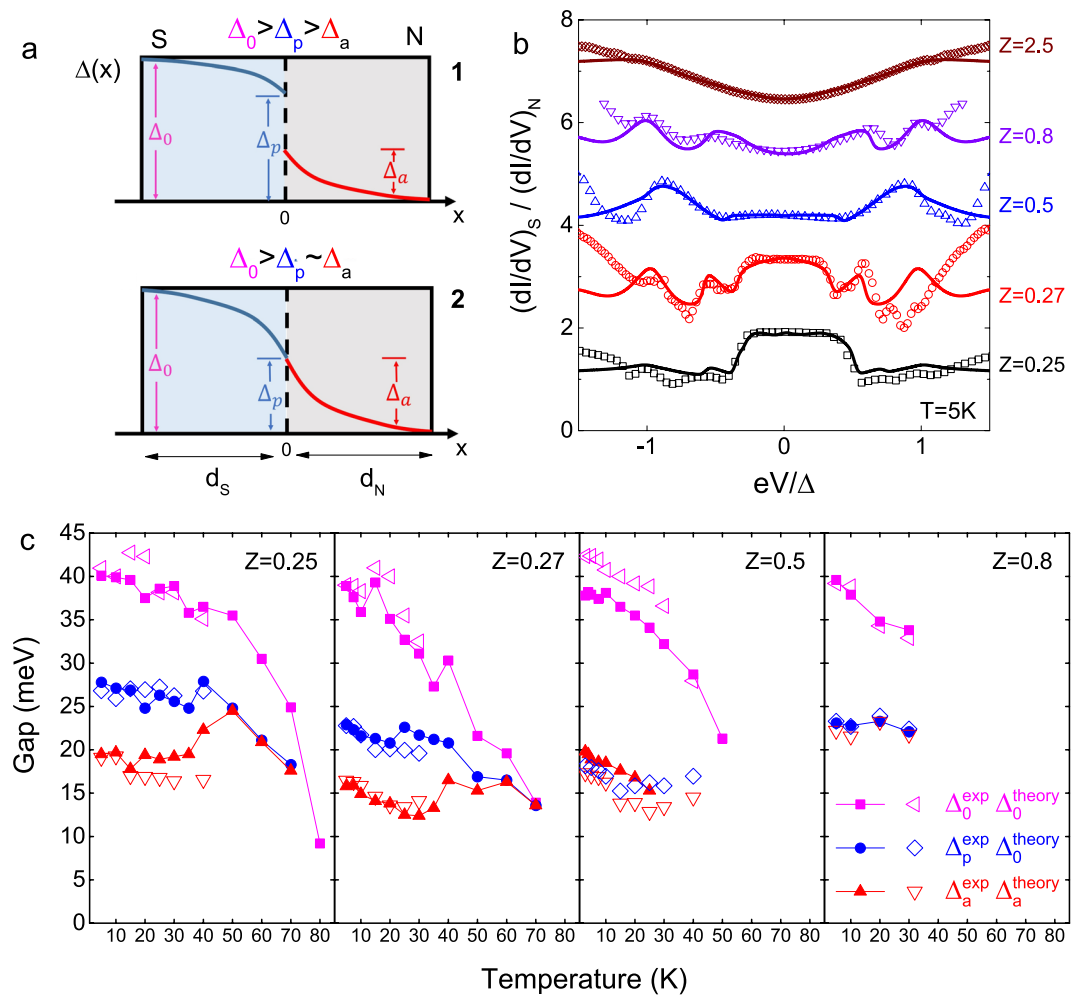


Figure 4. Superconducting proximity effect and theoretical modeling. **(a)** Schemes of NS junction with superconducting proximity effect. Δ_0 , Δ_p and Δ_a correspond to the intrinsic superconducting gap, depressed superconducting gap on S side at interface and induced superconducting gap on N side at the interface due to the superconducting proximity effect. Upper scheme: $\Delta_0 > \Delta_p > \Delta_a$; Lower scheme: $\Delta_0 > \Delta_p \sim \Delta_a$. **(b)** Calculated (colored solid lines) and measured (hollow symbols) normalized differential conductance $(dI/dV)_S / (dI/dV)_N$ at 5 K for various Bi-2212/1T-TaS₂ junctions, with BTK parameters $Z=0.25, 0.27, 0.5, 0.8$ and 2.5. The junction with $Z=2.5$ does not show any superconducting proximity effect at the NS interface. Curves are shifted for clarity. **(c)** Temperature dependence of Δ_0 , Δ_p and Δ_a for various Bi-2212/1T-TaS₂ junctions: Junction-1, $Z=0.25$; Junction-2, $Z=0.27$; Junction-3, $Z=0.5$; Junction-4, $Z=0.8$. More details are discussed in the text. The gaps used in the theoretical calculation of $(dI/dV)_S / (dI/dV)_N$ are marked as large-sized hollow symbols, and the gaps from measurements are marked as small-sized solid symbols.

From the linear DC I - V characteristics (seen in Figs 2(a) and S.5(a,b)), the normalized zero-bias conductance (NZBC) for Junction-1 with $Z=0.25$ divided by the conductance at 100 K is calculated and shown in Fig. 6(a) as a function of temperature for the cooling cycle. At high temperatures above T_c where the Bi-2212 is in the normal state, hysteresis dominates in the temperature range of 180 K to 230 K as it does in the four-terminal temperature-dependent resistance of a pristine 1T-TaS₂ flake shown in Supplementary Fig. S.1(b).

For additional insight, we use a back-to-back structured Ag/1T-TaS₂/Ag trilayer junction to detect the perpendicular transport characteristic of a metal/1T-TaS₂ junction. The linear I - V characteristics are shown in Fig. S.5(c,d). As shown in Fig. 6(b), the temperature-dependent NZBC of Ag/1T-TaS₂/Ag reveals the signature of the CDW transition in 1T-TaS₂ by a strong suppression of the NZBC when 1T-TaS₂ transits from a metallic NCCDW phase to a Mott-CCDW phase. In this case the metal/1T-TaS₂ junction is expected to include a metal/semiconductor barrier owing to the opened Mott gap of 1T-TaS₂ at low temperatures. Thus, the observed hysteresis in Junction-1 suggests the existence of CDW transitions when Bi-2212 is intimately contacted to 1T-TaS₂ either as a superconductor or a normal metal. In both cases the 1T-TaS₂ has clearly converted to a Mott-CCDW phase at low temperatures. Moreover, the NZBC of Junction-1 in panel (a) has increased with decreasing temperature up to almost 2 times that of the referenced 100 K conductance due to the Andreev reflection contributions at base temperature 5 K. Accordingly, the superconducting proximity effect and the CDW transition are simultaneously present in the same sample. We also note an obviously suppressed amplitude of the hysteresis window for

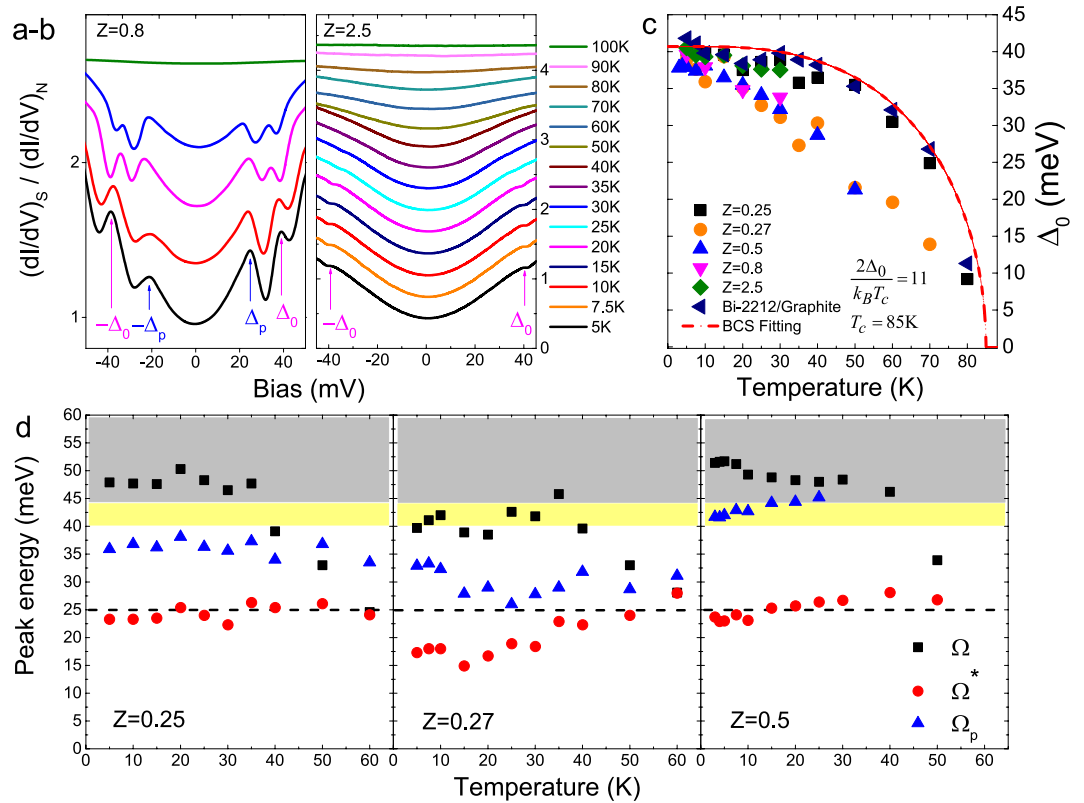


Figure 5. Junctions with lower transparencies, measured Bi-2212 intrinsic superconducting gap and boson mode energies in junctions. **(a,b)** Normalized differential conductance spectroscopies $(dI/dV)_S / (dI/dV)_N$ at various temperatures (5 K to 100 K) for Junction-4 (left, BTK $Z = 0.8$) and Junction-5 (right, BTK $Z = 2.5$). Curves are shifted for clarity. **(c)** Temperature dependent Bi-2212 intrinsic superconducting gap Δ_0 measured from various junctions, including Bi-2212/1T-TaS₂ and Bi-2212/graphite junctions. The red dashed line indicates the BCS fitting with a gap ratio $2\Delta_{sc}/k_B T_c = 11$. **(d)** Temperature dependence of boson mode energy $\Omega = E_p - \Delta_0$, $\Omega^* = E_p^* - \Delta_0$ and $\Omega_p = E_p - \Delta_p$ for Junction-1-3. At 5 K, Ω , Ω^* and Ω_p are: 48 meV, 24 meV and 36 meV for Junction-1; 40 meV, 17 meV and 33 meV for Junction-2; 51 meV, 24 meV and 41 meV for Junction-3. Gray background indicates the energy range from 44 meV to 60 meV, yellow background indicates the energy range from 40 meV to 44 meV, and black dashed line indicates the energy level of 25 meV. Note, the Ω_p for Junction-3 is calculated by the predicted value based on the modeling due to the difficulty of distinguishing Δ_p and Δ_a in Junction-3.

Junction-1 compared to the Ag/1T-TaS₂/Ag junction. Such a signature of suppression reveals the more metallic nature of 1T-TaS₂ when in contact with Bi-2212.

Consequently, the superconducting proximity effect observed in our highly transparent Bi-2212/1T-TaS₂ junctions strongly suggests that high- T_c superconductivity forms within the metastable metallic phase with a smaller parameter U/W , residing in the Mott-CCDW phases located in the topmost layers of 1T-TaS₂. The different heights and widths of the zero bias peak on the conductance characteristics for various Bi-2212/1T-TaS₂ junctions with different transparencies might be ascribed to the Andreev reflection corresponding to different configurations of Mott-CCDW phase and metallic phase in 1T-TaS₂ (See Supplementary information for more discussion). The curved and depressed zero-bias conductance peak (seen in Figs 2(b,d) and 3(b)) corresponds to the smearing effect with increasing quasiparticle scattering rate^{33,45}. Accordingly, it is no surprise that the quasiparticle lifetime parameters Γ_a at the interface on the N side (see Table 1) are lower by more than a factor of ten for the high transparency Junction 1 and 2 than they are for the lower transparency Junction 3 and 4.

We rule out alternative interpretations with the following arguments: Firstly, the Bi-2212 intrinsic superconducting gap Δ_0 measured from various Bi-2212/1T-TaS₂ and Bi-2212/graphite junctions shows consistency of the results at temperatures well below Bi-2212 T_c , with the BCS gap ratio $2\Delta_{sc}/k_B T_c$ to be around 10.4–11.5 (seen in Fig. 5(c)) in good agreement with previous works on intrinsic Bi-2212^{26,27}. Moreover, less dependence of the proximity induced gap Δ_a on temperature (seen in Fig. 4(c)) rules out a contribution to the differential conductance from *Andreev bound states caused by planar geometry or surface roughness*^{46–48}. (Here, we claim the larger deviation of measured superconducting gaps among various junctions at higher temperatures close to the T_c of Bi-2212 is probably due to distortion of gap features on conductance spectroscopies by stronger scattering and temperature smearing effects, which could be self-consistently verified by the smaller deviations of gap parameters used in theoretical results shown in Fig. S3(f)). Secondly, though there is a strong suppression of amplitude for the zero bias conductance peak for various junctions (almost two times the normal conductance in Junction-1

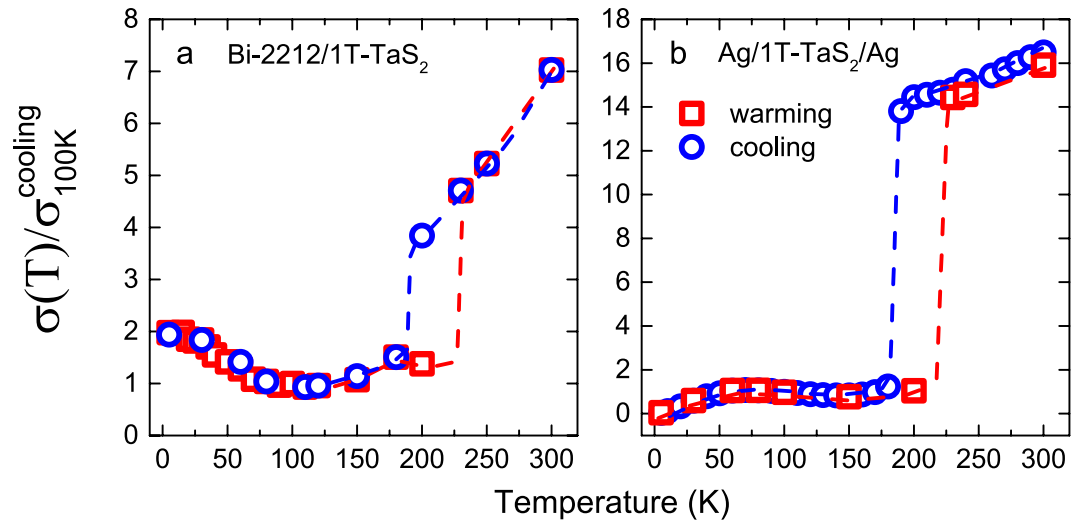


Figure 6. Normalized zero-bias conductance for (a) Bi-2212/1T-TaS₂ Junction-1 ($Z = 0.25$) and (b) Ag/1T-TaS₂/Ag junction plotted as a function of temperature under a cooling/warming cycle. The reference conductance is the zero-bias conductance at 100 K on the cooling cycle. The red and blue dashed lines indicate the CCDW-NCCDW transition of 1T-TaS₂.

and Junction-2, whereas 30% larger than normal conductance in Junction-3), less temperature dependence of the wide induced gap Δ_a (41% to 55% Δ_0 on 1T-TaS₂ side as shown in Fig. 4(c)) rules out the feature of the *complex Andreev reflection due to the phase conjugation of electrons and holes* predicted for superconductor-semiconductor interfaces⁴⁹. Thirdly, there is no dominant feature of periodic conductance peaks observed in any of our Bi-2212/1T-TaS₂ junctions, which rules out the possibility that our observed proximity feature is related to *McMillan-Rowell oscillation* observed in some normal metal/cuprate junctions^{31,50–53}. Lastly, with a very short *c*-axis coherence length ($\sim 1 \text{ \AA}$ ⁵⁴) in intrinsic Bi-2212, the absence of evidence for Josephson junctions intrinsically formed by superconducting CuO₂ and non-superconducting Bi-O and Sr-O layers^{55,56} observed at temperatures well below T_c rules out the explanation of the *superconducting proximity effect masquerading as interlayer tunneling* within the Bi-2212.

In Section IIB-2 we discussed the presence of two dip-hump structures, U_{e-ph} and U_{e-ph}^* which when associated with peak/dip features in the dI^2/dV^2 spectra at positive/negative bias regions defined respectively the energies E_p and E_p^* . We then referenced these features to the intrinsic Bi-2212 gap edge Δ_0 using the relations $\Omega = E_p - \Delta_0$ and $\Omega^* = E_p^* - \Delta_0$ and find that the temperature-dependent boson mode energy Ω is consistent with the STM spectrum on intrinsic Bi-2212⁴¹. This picture is incomplete however without comparing the energy of the second feature referenced to the intrinsic gap, $\Omega^* = E_p^* - \Delta_0$ and alternatively referenced to the reduced gap at the interface, Δ_p , using the relation $\Omega_p = E_p - \Delta_p$, revealing a slightly larger energy scale than Ω^* both of which are derived from E_p^* . For Junction 1–3 these three boson modes, Ω , Ω^* and Ω_p are plotted in Fig. 5(d) as a function of temperature.

Here, we provisionally assume the two dip-hump structures in conductance spectroscopies, observed in Junction-1–3, are due to self energy effects related to electron-boson interaction where phonons serve as the relevant bosons. We then infer that the “glue” assisting the strong-coupled pairing of electrons responsible for the high- T_c superconductivity in 1T-TaS₂ arises from phonons. The key point, here, is whether the additional hump peaked at U_{e-ph}^* is the hump corresponding to the suppressed superconducting gap Δ_p because of a boson mode energy Ω_p representing the difference between the junction interface and bulk Bi-2212, or a hump related to intrinsic superconducting gap Δ_0 due to a boson mode energy Ω^* incorporating the effect of interplay between electron-electron and electron-phonon interactions in 1T-TaS₂ on the density of states. For all junctions, the boson mode energy Ω at low meV is within the range of 40 meV to 60 meV (as indicated by the gray background) as well as being less temperature dependent. The results are consistent with the STM spectrum on intrinsic Bi-2212⁴¹. The yellow background demarcates the possible reduction ($\sim 4 \text{ meV}$ ⁴¹) due to the substitution of ¹⁶O by ¹⁸O in Bi-2212 crystals. Slightly lower energy Ω_p relative to Ω is observed in all Junction 1–3. On the other hand, all junctions reveal a nearly temperature-independent boson mode energy Ω^* around 25 meV indicated by the horizontal black dashed line (except Junction-2 over limited temperatures). The magnitude of Ω^* is in good agreement with the energy scale of an observed 25 meV infrared optical phonon⁵⁷ corresponding to a CDW near the same energy⁵⁸ that provides insight into the disorder-induced quasimetallic phase of 1T-TaS₂ residing in the Mott-CCDW phase. Additionally, the observed evolution of broader (Junction-1–2 as seen in Fig. 2) to sharper (Junction-3 as seen in Fig. 3) line-shape of the hump peaked at U_{e-ph}^* is consistent with current evidence and explanations of the transition from a Mott-insulating to a metallic phase in 1T-TaS₂ due to reduced Coulomb interaction U and broadened band width W of lower Hubbard band^{17–21,58}.

In conclusion, we have used differential conductance spectroscopy of Bi-2212/1T-TaS₂ junctions with varying transparencies to find high- T_c superconductivity induced within pristine 1T-TaS₂ by the proximity effect. The

CDW order in the 1T-TaS₂ appears to play an important role firstly by coexisting with an unexpected and surprisingly high T_c of the proximity gap in the 1T-TaS₂ and secondly by revealing a heretofore unseen ancillary dip-hump feature that accompanies a primary dip-hump feature corresponding to a boson (phonon) mode Ω previously seen in STM work on intrinsic Bi-2212. This second dip-hump feature is clearly related to the proximity of the CDW dominated 1T-TaS₂ and implies one of two possible boson modes depending on whether the dip-hump feature is referenced to the reduced gap Δ_p or the intrinsic gap Δ_0 at the interface. In the former case the temperature-dependent boson mode $\Omega_p = E_p^* - \Delta_p$ has values in the range 30–45 meV, somewhat less than the 40–50 meV range shown in Fig. 5(c) for Ω . The energy Ω_p can probably be interpreted as the mode relating to the gap Δ_p in the same manner as the mode Ω is related to the intrinsic gap Δ_0 . In the latter case however the temperature dependent boson mode $\Omega^* = E_p^* - \Delta_0$ has values in the range 20–25 meV which is close to the infrared active phonon mode associated with the CDW in 1T-TaS₂ as measured by infrared reflectance⁵⁷. This more plausible latter interpretation provides independent evidence that the phonon associated with the CCDW phase coexists with and may even enhance the superconductivity in pristine 1T-TaS₂. However, both of the above scenarios describing the second dip-hump structure provide reasonable rationales for the occurrence of a high- T_c proximity effect in Bi-2212/1T-TaS₂ junctions. Our work posits a mutual interaction of the CCDW and superconducting order parameters in the interfacial region of Bi-2212/1T-TaS₂ contacts, thereby revealing rich phenomenology and confirming a strong interplay between high T_c superconductivity and CDW order which is only beginning to be understood.

Methods

Sample fabrication. High quality, optimally doped single crystals of Bi₂Sr₂CaCu₂O_{8+ δ} (Bi-2212) were synthesized using the method of Mitzi *et al.*⁵⁹, with the modification that a Pt crucible was used in place of an alumina one. This avoided possible contamination of the melt via reaction with the crucible walls. Single crystals of 1T-TaS₂ flakes were prepared using iodine vapor transport⁶⁰. The transport measurements shown in Fig. S1 verify the critical superconducting temperature of Bi-2212 to be 85 K, and the CCDW-NCCDW transition temperatures for cooling and warming processes of 1T-TaS₂ to be 180 K and 230 K respectively. Prior to junction fabrication, thick flake Bi-2212 (thickness around 10 μ m) was mechanically exfoliated via Nitto-REVALPHA thermal release tape. Then, thick flake Bi-2212 was transferred to a clean glass substrate by thin double sided tape. Thin flake Bi-2212 (0.5 to 2 μ m) was then cleaved via Scotch tape. A cleaved thin flake of 1T-TaS₂ (2 to 5 μ m) was immediately placed against the cleaved surface of Bi-2212 after similar mechanical exfoliation. The two cleaved flakes strongly adhere to each other via Van der Waals forces, naturally forming high quality NIS or NS heterostructures. Junctions with different transparencies, characterized with theoretical modeling by the extended BTK model described in the manuscript, were randomly achieved. No significant dependence of the transparency upon area of junction or thickness of flake was recognized. All steps of fabrication were performed in a dry atmosphere, and all cleaved surfaces of thin flake Bi-2212 and 1T-TaS₂ were clean and flat. Based on multiple measured local-areas on the exfoliated pieces, the mean roughness for both materials is within 2 Å as indicated by the AFM images shown in Fig. 1(c). Also, to implement four-terminal *c*-axis differential conductance measurements, the thin flake Bi-2212 and 1T-TaS₂ were fashioned into narrow rectangular shapes oriented perpendicular to each other with an overlap area around 0.2 mm², as shown in Fig. 1(d).

Experimental measurements set-up. All measurements including the four-terminal AC differential conductance measurements and the DC current-voltage (*I*-*V*) measurements were performed over a wide range of temperature (2.5 K to 120 K) using a Quantum Design Physical Properties Measurement System (PPMS). Samples were mounted on a commercial PPMS puck and all measurements were performed in a low-noise screen room. For AC measurements, we used 23.3 Hz as the AC output frequency. The DC source voltage was supplied by a Keithley 2400 source meter and the AC source was supplied by a Agilent 33120 A AC generator with $\Delta V \sim 0.2$ mV. The DC and AC source signals were added using a homemade DC + AC adder and then applied to the junction. The DC bias across the junctions was measured with HP 3456A multimeter, the AC voltage signal with a SR830 DSP lock-in amplifier, and the AC current signal with a second SR830 lock-in amplifier after converting the current to a voltage using a SR570 current preamplifier.

Data normalization. For non-ideal NS junctions which have different density of states on the N and S sides, the conductance at one specific temperature cannot be simply normalized because of temperature dependence of the normal conductance. Thus, we normalized the AC differential conductance of non-ideal NS junctions, such as Junction-3, Junction-4 and Junction-5 discussed in the manuscript, by using the conductance at 100 K manually scaled into the range of the normal conductance at one specific temperature as the effective normal conductance. For instance, in Junction-3 the normal conductance at 5 K is around 0.2 μ A/mV and the conductance of the normal state at 100 K is around 0.4 μ A/mV. Hence, the ratio factor r_{eff} is the ratio of the normal conductance at 5 K to conductance at 100 K, which is around 0.5. Then, the normalized differential conductance spectroscopy at 5 K can be determined by multiplying a ratio factor r_{eff} when calculating the division of $(dI/dV)_S$ by $(dI/dV)_N$.

Data availability. The datasets generated during and/or analysed during the current study are available from the corresponding author on reasonable request.

References

- De Gennes, P. G. Boundary effects in superconductors. *Rev. Mod. Phys.* **36**, 225–237 (1964).
- Deutscher, G. Andreev Saint-James reflections: A probe of cuprate superconductors. *Rev. Mod. Phys.* **77**, 109–135 (2005).
- McMillan, W. L. Tunneling model of the superconducting proximity effect. *Phys. Rev.* **175**, 537–542 (1968).
- Zareapour, P. *et al.* Proximity-induced high-temperature superconductivity in the topological insulators Bi₂Se₃ and Bi₂Te₃. *Nat. Commun.* **3**, 1056 (2012).

5. Xu, J.-P. *et al.* Experimental detection of a majorana mode in the core of a magnetic vortex inside a topological insulator–superconductor Bi₂Se₃/NbSe₂ heterostructure. *Phys. Rev. Lett.* **114**, 017001 (2015).
6. Efetov, D. K. *et al.* Specular interband Andreev reflections at van der Waals interfaces between graphene and NbSe₂. *Nature Phys.* **12**, 328–332 (2016).
7. Straub, Th *et al.* Charge–Density–Wave mechanism in 2H–NbSe₂: Photoemission results. *Phys. Rev. Lett.* **82**, 4504–4507 (1999).
8. Chang, J. *et al.* Direct observation of competition between superconductivity and charge density wave order in YBa₂Cu₃O_{6.67}. *Nature Phys.* **8**, 871–876 (2012).
9. Sipos, B. *et al.* From Mott state to superconductivity in 1T-TaS₂. *Nat. Mater.* **7**, 960–965 (2008).
10. Ang, R. *et al.* Atomistic origin of an ordered superstructure induced superconductivity in layered chalcogenides. *Nat. Commun.* **6**, 6091 (2015).
11. Ang, R. *et al.* Real-space coexistence of the melted mott state and superconductivity in Fe-substituted 1T-TaS₂. *Phys. Rev. Lett.* **109**, 176403 (2012).
12. Yu, Y. *et al.* Gate-tunable phase transitions in thin flakes of 1T-TaS₂. *Nat. Nanotechnol.* **10**, 270–276 (2015).
13. Fazekas, P. In *Modern Trends in the Theory of Condensed Matter: Lecture Notes in Physics* vol. 115, 328–338 (Springer, 1980).
14. Fazekas, P. & Tosatti, E. Charge carrier localization in pure and doped 1T-TaS₂. *Physica B+C* **99**, 183187 (1980).
15. Thomson, R. E., Burk, B., Zettl, A. & Clarke, J. Scanning tunneling microscopy of the charge-density-wave structure in 1T-TaS₂. *Phys. Rev. B* **49**, 16899–16916 (1994).
16. Kim, J. J., Yamaguchi, W., Hasegawa, T. & Kitazawa, K. Observation of Mott localization gap using low temperature scanning tunneling spectroscopy in commensurate 1T-TaS₂. *Phys. Rev. Lett.* **73**, 2103–2106 (1994).
17. Ma, L. *et al.* A metallic mosaic phase and the origin of Mott-insulating state in 1T-TaS₂. *Nat. Commun.* **7**, 10956 (2016).
18. Cho, D. *et al.* Nanoscale manipulation of the Mott insulating state coupled to charge order in 1T-TaS₂. *Nat. Commun.* **7**, 10453 (2016).
19. Vaskivskiy, I. *et al.* Controlling the metal-to insulator relaxation of the metastable hidden quantum state in 1T-TaS₂. *Sci. Adv.* **1**, e1500168 (2015).
20. Hollander, M. J. *et al.* Electrically driven reversible Insulator–Metal phase transition in 1T-TaS₂. *Nano Lett.* **15**, 1861–1866 (2015).
21. Vaskivskiy, I. *et al.* Fast electronic resistance switching involving hidden charge density wave states. *Nat. Commun.* **7**, 11442 (2016).
22. Kashiwaya, S., Tanaka, Y., Koyanagi, M. & Kajimura, K. Theory for tunneling spectroscopy of anisotropic superconductors. *Phys. Rev. B* **53**, 2667–2676 (1996).
23. Geim, A. K. & Grigorieva, I. V. Van der Waals heterostructures. *Nature* **419–425** (2013)
24. Büttiker, M. Four-terminal phase-coherent conductance. *Phys. Rev. Lett.* **57**, 1761–1764 (1986).
25. Hebard, A. F. & Shumate, P. W. A new approach to high resolution measurements of structure in superconducting tunneling currents. *Rev. Sci. Instrum.* **529–533** (1974).
26. Renner, Ch, Revaz, Bernard, Kadowaki, K., Maggio-Aprile, K. I. & Fischer, Ø. Observation of the Low Temperature Pseudogap in the Vortex Cores of Bi₂Sr₂Ca₁Cu₂O_{8+δ}. *Phys. Rev. Lett.* **80**, 3606–3609 (1998).
27. Renner, Ch & Fischer, Ø. Vacuum tunneling spectroscopy and asymmetric density of states of Bi₂Sr₂Ca₁Cu₂O_{8+δ}. *Phys. Rev. B* **51**, 9208–9218 (1995).
28. Pannetier, B. & Courtois, H. Andreev reflection and proximity effect. *J. Low. Temp. Phys.* **118**, 599–615 (2000).
29. Blonder, G. E., Tinkham, M. & Klapwidijk, T. M. Transition from metallic to tunneling regimes in superconducting microconstrictions: Excess current, charge imbalance, and supercurrent conversion. *Phys. Rev. B* **25**, 4515–4532 (1982).
30. De Gennes, P. G. & Saint-James, D. Elementary excitations in the vicinity of a normal metal–superconducting metal contact. *Phys. Lett.* **4**, 151–152 (1963).
31. Wolf, E. L. Proximity electron tunneling spectroscopy. *Phys. Rep.* **91**, 31–102 (1982).
32. van Son, P. C., van Kempen, H. & Wyder, P. New method to study the proximity effect at the normal–metal–superconductor interface. *Phys. Rev. Lett.* **59**, 2226–2228 (1987).
33. Dynes, R. C., Narayanamurti, V. & Garno, J. P. Direct measurement of quasiparticle-lifetime broadening in a strong-coupled superconductor. *Phys. Rev. Lett.* **41**, 1509–1511 (1978).
34. Eschrig, M. & Norman, M. R. Neutron resonance: Modeling photoemission and tunneling data in the superconducting state of Bi₂Sr₂Ca₁Cu₂O_{8+δ}. *Phys. Rev. Lett.* **85**, 3261–3264 (2000).
35. Cuk, T. *et al.* Coupling of the B_{1g} phonon to the antinodal electronic states of Bi₂Sr₂Ca_{0.92}Y_{0.08}Cu₂O_{8+δ}. *Phys. Rev. Lett.* **93**, 11700 (2004).
36. Hashimoto, M. *et al.* Direct spectroscopic evidence for phase competition between the pseudogap and superconductivity in Bi₂Sr₂Ca₁Cu₂O_{8+δ}. *Nat. Mater.* **14**, 37–42 (2015).
37. McMillan, W. L. & Rowell, J. M. “Superconductivity”. **1** (ed. Parks, R. D.) 561 (Dekker, New York, 1969).
38. Scalapino, D. J. “Superconductivity”. **1** (ed. Parks, R. D.) 561 (Dekker, New York, 1969).
39. Carbotte, J. P. Properties of boson-exchange superconductors. *Rev. Mod. Phys.* **62**, 1027–1157 (1990).
40. Wolf, E. L. “Principles of Electron Tunneling Spectroscopy”, Oxford University Press, New York, Chapter 4 (1989).
41. Lee, J. *et al.* Interplay of electron-lattice interactions and superconductivity in Bi₂Sr₂Ca₁Cu₂O_{8+δ}. *Nature* **442**, 546–550 (2006).
42. Shen, Z. X., Spicer, W. E., King, D. M., Dessau, D. S. & Wells, B. O. Photoemission Studies of High-Tc Superconductors: The Superconducting Gap. *Science* **267**, 5296 (1995).
43. Ding, H. *et al.* Angle-resolved photoemission spectroscopy study of the superconducting gap anisotropy in Bi₂Sr₂Ca₁Cu₂O_{8+δ}. *Phys. Rev. B* **54**, R9678–R9681 (1996).
44. Norman, M. R. *et al.* Destruction of the Fermi surface in underdoped high-Tc superconductors. *Nature* **392**, 157160 (1998).
45. Plecenik, A., Grajcar, M., Beňačka, Š., Seidel, P. & Pfuch, A. Finite quasiparticle lifetime effects in the differential conductance of Bi₂Sr₂Ca₁Cu₂O_{8+δ}/Au junctions. *Phys. Rev. B* **49**, 10016–10019 (1994).
46. Hu, C.-R. Midgap surface states as a novel signature for d_{xa2–xb2}-wave superconductivity. *Phys. Rev. Lett.* **72**, 1526–1529 (1994).
47. Alfi, L. *et al.* Andreev bound states in high temperature superconductors. *Eur. Phys. J. B* **5**, 423–438 (1998).
48. Barash, Y. S., Svidzinsky, A. A. & Burkhardt, H. Quasiparticle bound states and low-temperature peaks of the conductance of NIS junctions in d-wave superconductors. *Phys. Rev. B* **55**, 15282 (1997).
49. van Wees, B. J., de Vries, P., Magnée, P. & Klapwijk, T. M. Excess conductance of superconductor–semiconductor interfaces due to phase conjugation between electrons and holes. *Phys. Rev. Lett.* **69**, 510–513 (1992).
50. Rowell, J. M. & McMillan, W. L. Electron interference in a normal metal induced superconducting contacts. *Phys. Rev. Lett.* **16**, 453–456 (1966).
51. Chang, H.-S., Bae, M.-H. & Lee, H.-J. McMillan–Rowell oscillations observed in c-axis Au/Bi₂Sr₂Ca₁Cu₂O_{8+δ} junctions. *Physica C* **408**, 618–619 (2004).
52. Shkedy, L., Aronov, P., Koren, G. & Polturak, E. Observation of McMillan–Rowell like oscillations in underdoped YBa₂Cu₃O_y junctions oriented along the node of the d–wave order parameter. *Phys. Rev. B* **69**, 132507 (2004).
53. Neshor, O. & Koren, G. Measurements of Δ and v_F from Andreev reflections and McMillan–Rowell oscillations in edge junctions of YBa₂Cu₃O_{6.6}/YBa₂Cu_{2.55}Fe_{0.45}O_y/YBa₂Cu₃O_{6.6}. *Phys. Rev. B* **60**, 9287–9290 (1999).
54. Palstra, T. T. M., Batlogg, B., Schneemeyer, L. F., Van Dover, R. B. & Waszczak, J. V. Angular dependence of the upper critical field of Bi_{2.2}Sr₂Ca_{0.8}Cu₂O_{8+δ}. *Phys. Rev. B* **38**, 5102–5105 (1988).

55. Kleiner, R., Steinmeyer, F., Kunkel, G. & Müller, P. Intrinsic Josephson effects in $\text{Bi}_2\text{Sr}_2\text{Ca}_1\text{Cu}_2\text{O}_8$ single crystals $\text{Bi}_2\text{Sr}_2\text{Ca}_1\text{Cu}_2\text{O}_{8+\delta}$. *Phys. Rev. Lett.* **68**, 2394–2397 (1992).
56. Kleiner, R. & Müller, P. Intrinsic Josephson effects in high- T_c superconductors. *Phys. Rev. B* **49**, 1327–1341 (1994).
57. Gasparov, L. V. *et al.* Phonon anomaly at the charge ordering transition in 1T-TaS₂. *Phys. Rev. B* **66**, 094301 (2002).
58. Cho, D., Cho, Y.-H., Cheong, S.-W., Kim, K.-S. & Yeom, H. W. Interplay of electron–electron and electron–phonon interactions in the low-temperature phase of 1T-TaS₂. *Phys. Rev. B* **92**, 085132 (2015).
59. Mitzi, D. B., Lombardo, L. W., Kapitulnik, A., Laderman, S. S. & Jacowitz, R. D. Growth and properties of oxygen- and ion-doped $\text{Bi}_2\text{Sr}_2\text{CaCu}_2\text{O}_{8+\delta}$ single crystals. *Phys. Rev. B* **41**, 6564–6574 (1990).
60. Gamble, F. R., Osiecki, J. H. & Di Salvo, F. J. Some superconducting intercalation complexes of TaS₂ and substituted pyridines. *J. Chem. Phys.* **55**, 3525–3530 (1971); Di Salvo, F. J., Hull, W. G., Jr., Schwartz, L. H., Voorhoeve, J. M. & Waszczak, J. V. Metal intercalation compounds of TaS₂: preparation and properties. *J. Chem. Phys.* **59**, 1922–1929 (1973).

Acknowledgements

The authors thank C. Samouche for the AFM measurements, A. G. Rinzler for supporting the related AFM facility and P. J. Hirschfeld for useful discussions. This work was supported by the National Science Foundation under Grant No. DMR–1305783 (AFH) and the Department of Energy under Grant No. DE-FG02-86ER45268 (GRS).

Author Contributions

A.J.L. and A.F.H. conceived and planned the research. A.J.L. and X.Z. implemented the measurement set-up and device fabrication. G.R.S. synthesized the high quality crystals of Bi-2212 and 1T-TaS₂. A.J.L. performed the measurements. X.Z. helped with the measurements. A.J.L. carried out the theoretical modeling and calculation. A.J.L. and A.F.H. wrote the paper with input from all authors. A.F.H. supervised the work. All the authors contributed and agreed to the scientific discussion and manuscript revision.

Additional Information

Supplementary information accompanies this paper at doi:10.1038/s41598-017-04645-1

Competing Interests: The authors declare that they have no competing interests.

Publisher's note: Springer Nature remains neutral with regard to jurisdictional claims in published maps and institutional affiliations.



Open Access This article is licensed under a Creative Commons Attribution 4.0 International License, which permits use, sharing, adaptation, distribution and reproduction in any medium or format, as long as you give appropriate credit to the original author(s) and the source, provide a link to the Creative Commons license, and indicate if changes were made. The images or other third party material in this article are included in the article's Creative Commons license, unless indicated otherwise in a credit line to the material. If material is not included in the article's Creative Commons license and your intended use is not permitted by statutory regulation or exceeds the permitted use, you will need to obtain permission directly from the copyright holder. To view a copy of this license, visit <http://creativecommons.org/licenses/by/4.0/>.

© The Author(s) 2017